

# A new analysis method for very high definition Imaging Atmospheric Cherenkov Telescopes as applied to the CAT telescope

S. Le Bohec<sup>c</sup> B. Degrange<sup>d</sup> M. Punch<sup>c</sup> A. Barrau<sup>e</sup>  
 R. Bazer-Bachi<sup>b</sup> H. Cabot<sup>g,4</sup> L.M. Chounet<sup>d</sup> G. Debiais<sup>g</sup>  
 J.P. Dezalay<sup>b</sup> A. Djannati-Ataï<sup>e</sup> D. Dumora<sup>a</sup> P. Espigat<sup>c</sup>  
 B. Fabre<sup>g</sup> P. Fleury<sup>d</sup> G. Fontaine<sup>d</sup> R. George<sup>e</sup> C. Ghesquière<sup>c</sup>  
 P. Goret<sup>f</sup> C. Gouiffes<sup>f</sup> I.A. Grenier<sup>f,i</sup> L. Iacoucci<sup>d</sup> I. Malet<sup>b</sup>  
 C. Meynadier<sup>g</sup> F. Munz<sup>c,h</sup> T.A. Palfrey<sup>j</sup> E. Paré<sup>d</sup> Y. Pons<sup>e</sup>  
 J. Québert<sup>a</sup> K. Ragan<sup>a</sup> C. Renault<sup>f,i</sup> M. Rivoal<sup>e</sup> L. Rob<sup>h</sup>  
 P. Schovaneck<sup>k</sup> D. Smith<sup>a</sup> J.P. Tavernet<sup>e</sup> J. Vrana<sup>d,4</sup>

<sup>a</sup>*Centre d'Etudes Nucléaire de Bordeaux-Gradignan, France<sup>1</sup>*

<sup>b</sup>*Centre d'Etudes Spatiales des Rayonnements, Toulouse, France<sup>2</sup>*

<sup>c</sup>*Laboratoire de Physique Corpusculaire et Cosmologie, Collège de France, Paris, France<sup>1</sup>*

<sup>d</sup>*Laboratoire de Physique Nucléaire de Haute Energie, Ecole Polytechnique, Palaiseau, France<sup>1</sup>*

<sup>e</sup>*LPNHE, Laboratoire de Physique Nucléaire de Haute Energie, Universités de Paris VI/VII, France<sup>1</sup>*

<sup>f</sup>*Service d'Astrophysique, Centre d'Etudes de Saclay, France<sup>3</sup>*

<sup>g</sup>*Groupe de Physique Fondamentale, Université de Perpignan, France<sup>1</sup>*

<sup>h</sup>*Nuclear Center, Charles University, Prague, Czech Republic*

<sup>i</sup>*Université Paris VII, France*

<sup>j</sup>*Department of Physics, Purdue University, Lafayette, IN 47907, U.S.A.*

<sup>k</sup>*Joint Laboratory of Optics Ac. Sci. and Palacky University, Olomouc, Czech Republic*

---

## Abstract

A new method of shower-image analysis is presented which appears very powerful as applied to those Cherenkov Imaging Telescopes with very high definition imaging capability. It provides hadron rejection on the basis of a single cut on the image shape, and simultaneously determines the energy of the electromagnetic shower and the position of the shower axis with respect to the detector. The source location is

also reconstructed for each individual  $\gamma$ -ray shower, even with one single telescope, so for a point source the hadron rejection can be further improved. As an example, this new method is applied to data from the CAT (Cherenkov Array at Thémis) imaging telescope, which has been operational since Autumn, 1996.

*Key words:* Gamma-Ray Astronomy, Atmospheric Cherenkov detector

---

## 1 Introduction

Most of the recent progress in ground-based  $\gamma$ -ray Astronomy has been obtained from Atmospheric Cherenkov Telescopes (ACT) using the imaging technique, which permits efficient rejection of the large background of proton or nucleus-induced showers. The utility of high-definition imaging has been demonstrated by the results obtained with the Whipple (109 pixels) [1], CANGAROO (220 pixels) [2], and HEGRA (271 pixels) [3] ACT's, leading to the discovery of several firmly established very-high-energy sources; e.g., the Crab nebula [4], the pulsar PSR 1706-44 [5], and the two relatively nearby Active Galactic Nuclei, Markarian 421 [6] and Markarian 501 [7]. Using a camera with a large number of small pixels allows a more profound image analysis than the usual procedure based on the first and second moments of the light distribution [8], with improved background rejection and energy resolution. The new image analysis described here takes advantage of the full imaging information, including the detailed longitudinal development of the shower (with a significant asymmetry between the top and the bottom of the shower) as well as its lateral extension. This method is based on an analytical model giving, for a genuine  $\gamma$ -ray shower, the average distribution of Cherenkov light in the focal plane as a function of the following parameters:  $\gamma$ -ray energy  $E_\gamma$ , distance  $D$  between the shower axis and the telescope (or impact parameter), the source position (defined by the vector  $\vec{\xi}$  in the focal plane), and the azimuthal position  $\phi$  of the shower image about the source in the focal plane. This model is used to define a  $\chi^2$ -like function of  $E_\gamma$ ,  $D$ ,  $\vec{\xi}$ , and  $\phi$ . For each observed shower, this function is minimized with respect to the parameters: the minimized  $\chi^2$  provides gamma-hadron discrimination; the  $\gamma$ -ray energy determination automatically takes account of the impact parameter which is obtained from the same fit. With this method, the origin of a genuine  $\gamma$ -ray shower can be reconstructed even with one single telescope. This result stems

---

<sup>1</sup> IN2P3/CNRS

<sup>2</sup> INSU/CNRS

<sup>3</sup> DAPNIA/CEA

<sup>4</sup> Deceased

from the fact that electromagnetic showers whose energies are known have a well-defined longitudinal development with rather small fluctuations. In the focal plane of an imaging ACT, this gives a well-defined longitudinal profile for the image, which depends on the impact parameter and angular origin of the shower. Therefore, the simultaneous measurement of  $E_\gamma$  and  $D$  in the preceding fit also yields the source position  $\vec{\xi}$ . For the case of a well-localized point source, the energy resolution can be improved by fixing the source position during the fit since there are fewer parameters in the fit.

In this article, the preceding method is illustrated as applied to the CAT imaging telescope [9], operating since Autumn 1996 in the French Pyrenees. Its very-high-definition imaging camera comprises a central region consisting of 546 phototubes in a hexagonal matrix spaced by  $0.13^\circ$ ; this is surrounded by 54 tubes in two “guard rings”. The angular diameter of the full field of view is  $4.8^\circ$  ( $3.0^\circ$  for the small pixels). The guard rings were installed in June 1997, so for the data and simulations used here, they are not included. A more complete description of the CAT imaging telescope can be found in [9]. The detector response has been simulated in detail, thus allowing the optimization of the new image analysis on the basis of Monte-Carlo-generated  $\gamma$ -showers against the background of real off-source data.

Section 2 is devoted to the full simulation of the instrument, allowing the calculation of the variation of the equivalent detection area as a function of  $E_\gamma$  for different zenith angles, thus defining the corresponding energy thresholds. In Section 3, the semi-analytical model giving the average Cherenkov light distribution in the focal plane for a  $\gamma$ -ray shower is described in detail and shown to be consistent with results from complete simulations of electromagnetic cascades. In Section 4, the performance of the analysis method is presented for different values of the zenith angle; the discussion is focused on hadron rejection by a single cut on the image shape (and for a known point source, an additional cut on direction), on the accuracy of the source location, and finally on energy resolution.

## 2 Simulation of the detector response

The development of electromagnetic or hadronic air showers in the atmosphere is simulated by a modified version of the program described in [10]. For each event, the Cherenkov photons falling onto the mirror elements are followed individually according to their arrival times, initial directions, and wavelengths; reflection from the Davies-Cotton mirror is calculated, taking into account imperfections of the mirrors’ shapes and orientations. Typical aberration images from a point source are smaller than or comparable to the pixel size. A wavelength-dependent fraction of photons is kept, reproducing the effect

of mirror reflectivity and Winston cones' efficiency [11] as well as phototubes' quantum efficiency. Photons from the sky-noise are also simulated, taking into account the effect of AC coupling on the read-out electronics. The contribution of typical star fields may be superposed. The time-structure and amplitude fluctuation of the pulses generated by single  $\gamma$ e's have been parametrized on the basis of tests with the CAT electronics. The signal from a given pixel is obtained from the pile-up of the contributions from individual  $\gamma$ e's according to their respective arrival times, taking account of the amplitude fluctuation of  $\sim 0.4\gamma$ e. The comparator threshold is set at a level corresponding to three times the height of the average single- $\gamma$ e signal. When a trigger occurs, the phototube signal (corrected for the effect of propagation along the 28 m cable) is integrated over the 12 ns time window provided by the fast gate, thus yielding the simulated ADC output. These ADC outputs are then used as input to the analysis procedure described in the following sections.

The preceding simulation of instrumental effects allows the calculation of the equivalent detection area for  $\gamma$ -rays as a function of energy for a given zenith angle  $Z$ . This is shown in Fig. 1.a for  $Z$ s of  $0^\circ$ ,  $30^\circ$ ,  $45^\circ$ , and  $60^\circ$ . Fig. 1.b shows the corresponding event rates of  $\gamma$ -rays for a reference source with the intensity and spectrum of the Crab nebula, as measured by the CAT telescope [12]:

$$\frac{d\phi}{dE} = 2.46 \times \left( \frac{E}{\text{TeV}} \right)^{-2.55} \times 10^{-11} \text{ cm}^{-2}\text{s}^{-1}\text{TeV}^{-1} \quad (1)$$

The energy corresponding to the maximum event rate ("mode energy") will be considered as the nominal threshold of the telescope; it varies from 250 to 350 GeV between zenith and  $Z = 30^\circ$  and increases to  $\approx 700$  GeV for  $Z = 45^\circ$ . Examples of real images from a  $\gamma$ -ray candidate shower and from hadron showers are shown in Fig. 2. Whereas  $\gamma$ -rays produce thin elongated images (Fig. 2.a), patterns from hadron showers are often more chaotic or patchy due to the superposition of several electromagnetic components due to  $\pi^0$ 's (Fig. 2.b and 2.c) and to Cherenkov rings or arcs generated by muons falling onto the mirror or close ( $< 40$  m) to the telescope (Fig. 2.d). For hadron showers with energies lower than 200 GeV, often the only component which is seen is the Cherenkov light from a single muon; such muons are a source of background in the case where the image is reduced to a short arc, which mimics a low-energy  $\gamma$ -ray shower [13]. It should be noted, however, that the CAT imaging telescope is surrounded by the seven detectors of the ASGAT timing array [14] (whose collectors are 7 m diameter each) which should permit the rejection of most of these background events when it resumes operation after upgrade, in 1998.

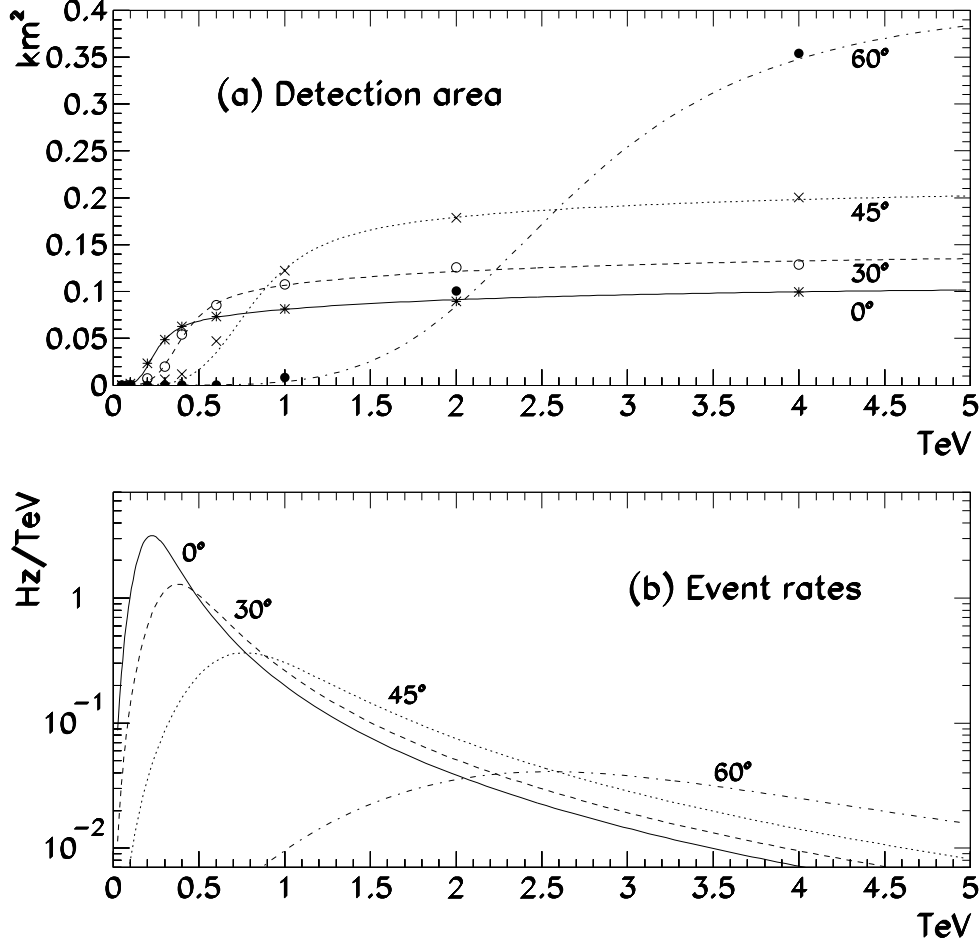


Fig. 1. a) Equivalent detection area for  $\gamma$ -rays as a function of energy for various values of zenith angle. The points show the values at which the acceptance was evaluated from Monte Carlo simulations, the curves are a fit to these points. b) Corresponding event rates per energy interval for  $\gamma$ -rays from a Crab-like source with a spectrum as given in Equation (1).

### 3 Modelling of $\gamma$ -shower images and image analysis method

For a given value of energy  $E_\gamma$  and impact parameter,  $D$ , the Cherenkov image of an electromagnetic shower fluctuates about the mean image, as a result both of intrinsic fluctuations of the shower and of statistical effects in the Cherenkov light collection, as well as instrumental fluctuations. An analysis based on the comparison between individual event images and the theoretical mean image as a function of impact parameter and energy allows full advantage to be taken of the high definition of the CAT imaging telescope camera. Such an analysis requires an analytical model for  $\gamma$ -shower Cherenkov images.

In order to construct this model, we have used the results from a paper by Hillas [15] in which the mean development of electromagnetic showers is described and parametrized on the basis of Monte-Carlo simulations. The num-

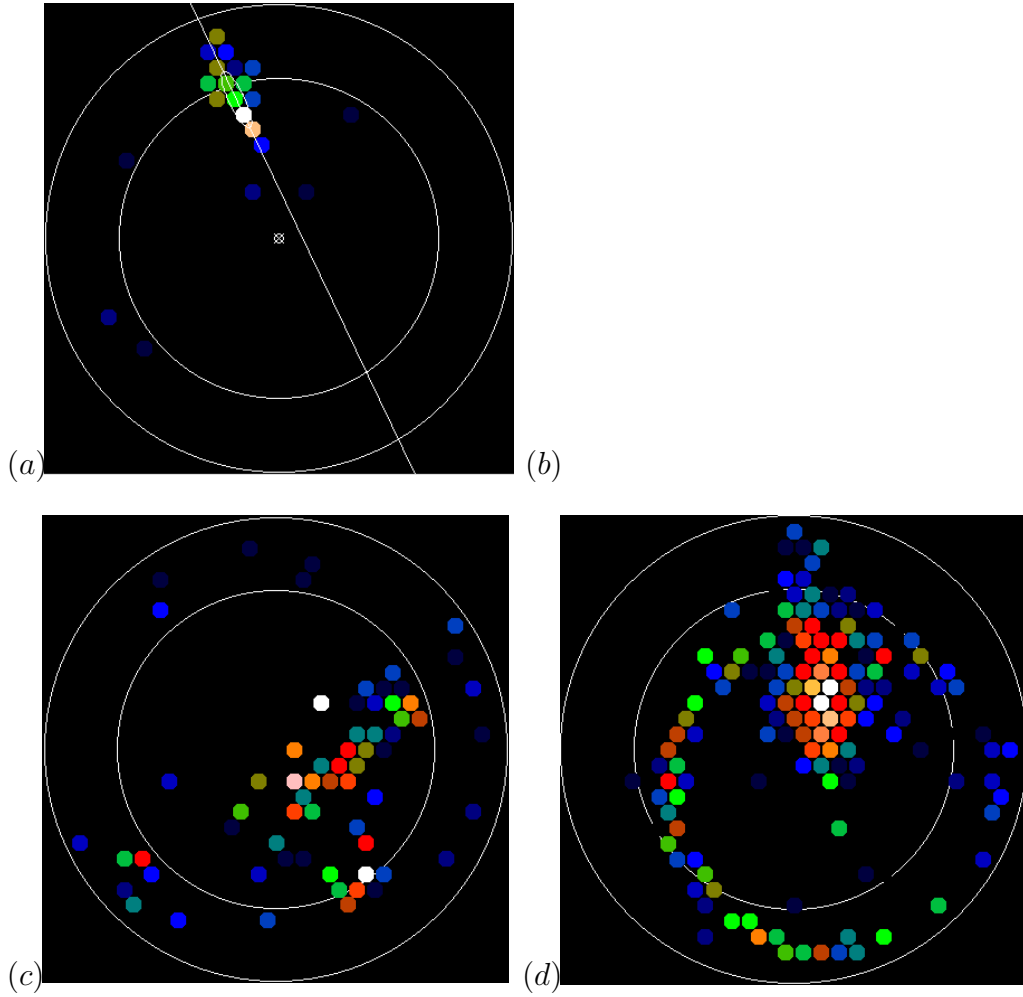


Fig. 2. Real shower images in the CAT imaging telescope: a)  $\gamma$ -ray shower candidate (estimated energy 620 GeV); b) and c) hadronic images; d) hadronic image with a characteristic muon arc. The concentric circles represent the trigger region and the small-pixel region, respectively.

ber of charged particles ( $e^\pm$ ) at a given atmospheric depth is given by the Greisen formula. Their energy spectrum and the angular distribution of their momenta with respect to the shower axis are given. Their spatial distribution around the shower axis is not explicitly stated, but parametrizations of their mean distance from this axis and of their spreads in the radial and azimuthal directions are given as a function of their energy and momentum angle. These parametrizations have been compared with our Monte-Carlo simulations, and were found to be in very good agreement, except for the mean value of the angular distribution which we have modified slightly (see Appendix 1). This description of the mean shower development permits the mean Cherenkov image to be deduced, with the additional use of the atmospheric density profile as in [10], optical absorption as in [16], Cherenkov emission properties, and some of the detector characteristics such as its light-collecting area, photo-tube

quantum efficiency as a function of wavelength, and site altitude. The angular distance from the source to the zenith has also to be taken into account.

In practice, the shower (for a given energy and impact parameter) is divided into “slices” perpendicular to its axis at different depths, and the contribution of each slice to the image is calculated. In such a slice, the contribution of a charged particle ( $e^\pm$ ) with a given energy and direction and a given lateral position with respect to the shower axis is evaluated as follows: the corresponding cone of Cherenkov emission traces a circle on the plane perpendicular to the shower axis containing the imaging telescope; rather than considering a mirror with a fixed position with respect to the shower, we allow it to rotate around the shower axis (the distance  $D$  is fixed) and use the intersection of the corresponding ring with the circle of Cherenkov light to find the average contribution of these  $e^\pm$ ’s to the image as well as the position of the photo-electrons in the focal plane (see Appendix 2 and Fig. 13). Summing over the energy, direction, and averaging over the lateral position of all  $e^\pm$ ’s in the slice gives the mean position of its image in the focal plane, its mean transverse extension, and the corresponding density of  $\gamma$ e’s. The sum of the contributions of all the slices gives a full mean image description in terms of the linear density of light along the image axis and the transverse extension of the image as a function of position along this axis. The form of the transverse profile is taken to be a constant shape, determined from Monte-Carlo simulations. This form is scaled to the calculated transverse extension, which varies with position along the image axis. The bi-dimensional profile of vertical 500 GeV  $\gamma$ -ray showers thus obtained is shown in Fig. 3 for different values of the impact parameter  $D$ . It can be seen that the longitudinal profiles of the expected images are asymmetrical and that their position and general shape depend on  $D$ . The consistency between this analytical calculation and the full Monte-Carlo simulation can be checked in Fig. 4, which shows the lateral and longitudinal profiles of the  $\gamma$ -images for various impact parameters, both from full Monte Carlo simulations and as given by the model. It can also be seen in Fig. 5, which shows the mean density of Cherenkov light on the ground in a  $4.6^\circ$  acceptance calculated by both methods, and found to be in good agreement.

For the comparison with an individual event image, the expected distribution of  $\gamma$ e’s in the focal plane (for given values of  $E_\gamma$ ,  $D$ , and  $\phi$  of the shower axis projected in the image plane) is integrated over each pixel area, according to the source angular position (defined by two angular coordinates  $\vec{\xi}$ ). A function  $\chi^2(E_\gamma, D, \vec{\xi}, \phi)$  is then defined in such a way that its minimization with respect to  $E_\gamma$ ,  $D$ ,  $\vec{\xi}$ , and  $\phi$  gives the values of those parameters which best fit the model to the image. This function is a sum of squared differences between expected and actual pixel contents divided by a quadratic error, extending over all the pixels whose expected or actual content is above a given threshold ( $2 \gamma e$ ). In the following expression,  $Q_i^{\text{real}}$  is the actual value of the charge

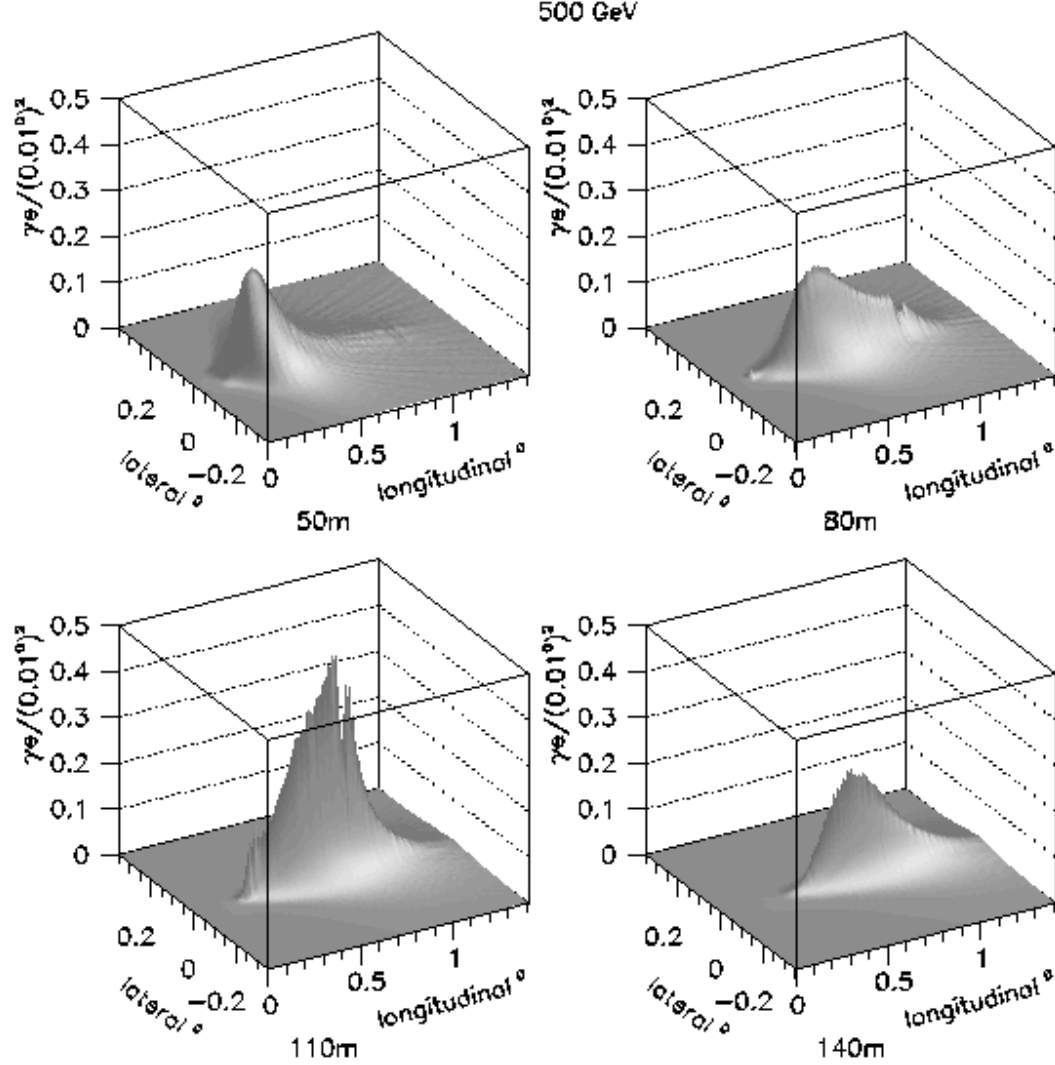


Fig. 3. Bidimensional image profiles of 500 GeV vertical  $\gamma$ -showers ( $\gamma_e$  density) for various values of impact parameter as given by the semi-analytical model. The  $x$  (longitudinal) and  $y$  (lateral) axes are coordinates in the focal plane in degrees. The source is at the origin. Note that the lateral scale is dilated by a factor of two.

collected in pixel  $i$  (measured in equivalent number of photo-electrons),  $Q_i^{\text{mean}}$  is the expected mean contribution of the shower to pixel  $i$  for a given set of model parameters, and  $\overline{B}_i$  is the mean contribution of the noise calculated on the basis of measured randomly-gated events, which contributes to the fluctuations but not to the charge, due to the AC coupling. For the CAT detector, the electronic noise dominates the night-sky background, since the mirror and pixel size are small and the gate is short. The fluctuations in  $Q_i^{\text{real}}$  and  $Q_i^{\text{mean}}$  are supposed proportional to the square root of the charge in the pixel, giving:

$$\chi^2 = \frac{1}{k} \sum_i \frac{(Q_i^{\text{real}} - Q_i^{\text{mean}})^2}{\overline{B}_i + \frac{1}{2}(Q_i^{\text{real}} + Q_i^{\text{mean}})}$$



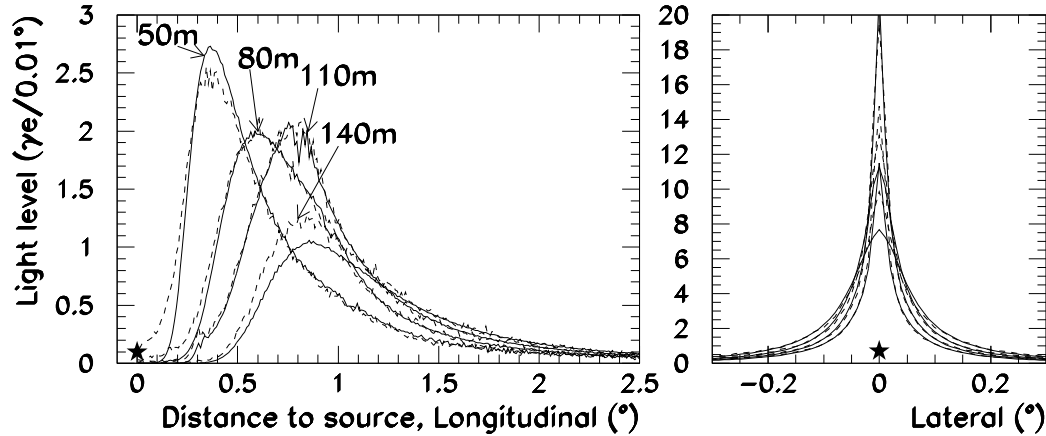


Fig. 4. Longitudinal and lateral image profiles ( $\gamma e$  density projected on the lateral/longitudinal axis) of 500 GeV vertical  $\gamma$ -showers for various values of impact parameter ( $D$ ). The source is at the position of the star. The image profiles as given by the semi-analytical model are shown by the full lines, the average image profiles from full Monte Carlo simulations by dotted lines. For the lateral profiles, the width of the profile decreases with increasing  $D$ .

The preceding expression is not a  $\chi^2$  *stricto sensu* since the exact number of degrees of freedom depends somewhat on the value of the fitted parameters through the number of expected hit photo-tubes. The value of the error factor  $k$  (here taken as 2.9) has no effect on the value of the fitted shower parameters. It has been adjusted on simulations in order to have an approximately flat  $\chi^2$  probability for simulated  $\gamma$ -shower images well above the trigger threshold. The use of an energy or impact parameter dependent  $k$ -value is under study. In the case of well-localized point sources, fits in which  $\vec{\xi}$  is fixed are used for improved energy resolution.

The fit is quite sensitive to the starting values, so a good estimation of these values is needed. For this purpose the usual moment-based parameters are calculated, but after a “principal cluster” image-cleaning procedure. In this procedure the pixels with a charge less than a threshold of  $2\gamma e$  are zeroed; the principal cluster consists of the largest number of contiguous pixels, all others are then zeroed. This provides moment-based parameters for  $\gamma$ -images which are more stable against the noise background (though these would not be useful for background rejection, as this cleaning procedure makes the hadronic background more “ $\gamma$ -like”). Relations between the moment-based parameters and the values to be fitted have been defined on Monte-Carlo simulations; these are then used to define the starting values for the fit.

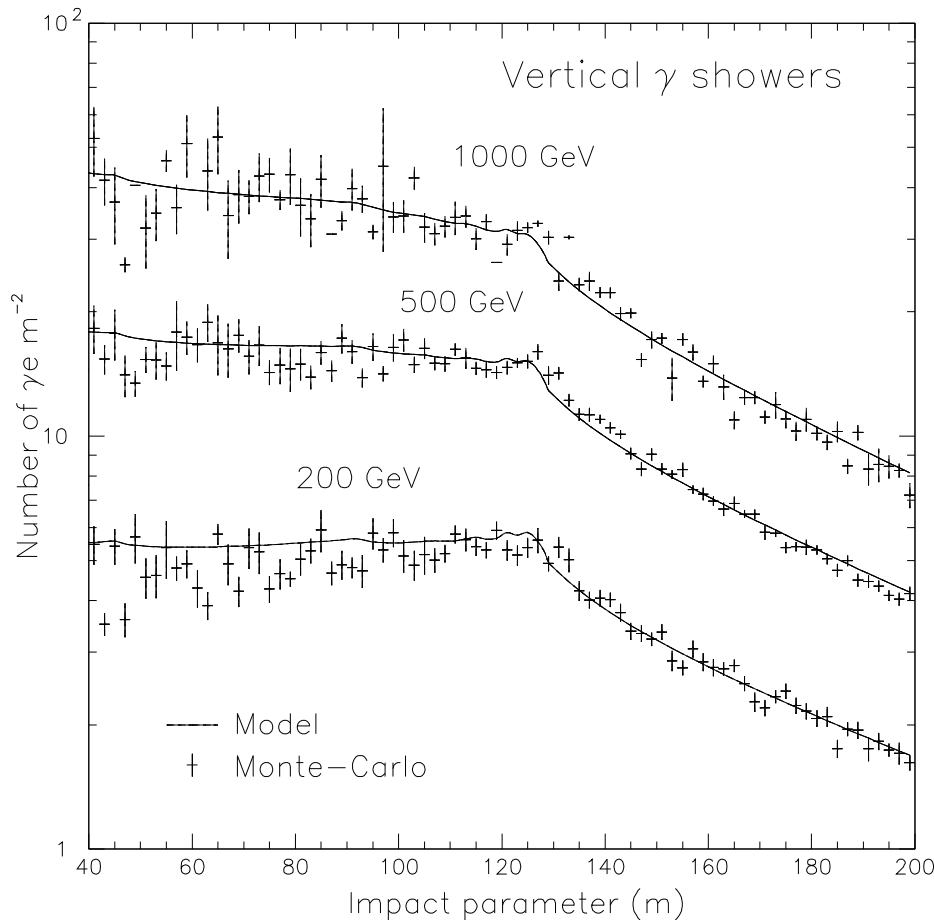


Fig. 5. Density of detected photons on the ground as a function of the impact parameter: the full line corresponds to the semi-analytic model described in the text; points with error bars show the result of full Monte Carlo simulations.

#### 4 Results of the method when applied to the CAT images

Many of the sources in the EGRET catalogue [17] have well-identified radio, optical, or X-ray counterparts, which give the source position to an accuracy much better than can be achieved by ACT telescopes. Such sources with known position are usually placed at the centre of the field of an imaging telescope. However, many unidentified sources in the EGRET catalogue are located in error boxes with typical size of  $1^\circ$ . Ground-based Cherenkov detectors are, in principle, able to localize such sources with a higher precision. In order to observe these sources, different methods have been developed by imaging Cherenkov telescope groups. Stereoscopy is the most direct way to find the direction of a source, but requires at least two telescopes and reduces the collection area [3]. For single-telescope experiments with sufficient background rejection on an image-shape criterion, it is possible to perform de-localized analyses assuming the source at the different points of a grid covering the field of view or by examining the distribution of the intersections of the image axes

[18]. However, an event-by-event analysis method such as that described here is preferable since in the former methods the signal is more easily drowned-out by the background.

The method has been tested on simulated  $\gamma$ -images provided by the Monte-Carlo simulation program described above and a realistic simulation of the detector response, including the measured variation in collection efficiency and gain between the phototubes, and measured wavelength response of the mirrors and Winston cones. For optimization of the cut values, these simulated  $\gamma$ -images have been used together with the real background events from data from off-source runs with the CAT imaging telescope. Gammas from a point-like source with the Crab nebula spectrum [12] (see equation (1) above) were simulated at various elevations. The capability of the method both for source detection and for source spectrum measurement have been examined.

#### 4.1 Source detection

As applied to the data, the method consists of minimizing the  $\chi^2$  with respect to  $E_\gamma$ ,  $D$ ,  $\vec{\xi}$ , and  $\phi$ . Fig 6 shows the  $\chi^2$  probability distributions obtained with this fit for the simulated  $\gamma$ -ray events and real background events. A cut on the  $\chi^2$  probability value,  $P(\chi^2)$ , provides a selection of  $\gamma$ -like events on the basis of the image shape alone. The reconstructed angular origins obtained for simulated  $\gamma$ -events accumulate around the actual source position which in this case is at the centre of the field. The dispersion around the actual source position has a typical RMS spread of  $0.14^\circ$ . For each event, the accuracy of the angular origin determination is better by a factor two in the direction perpendicular to the image axis than in the direction of the image axis (Fig. 7). The RMS longitudinal error typically varies from  $0.2^\circ$  to  $0.1^\circ$  as the energy varies from the threshold to 2 TeV. The angular origins obtained for background events are spread over the whole field with an approximately Gaussian distribution with a  $1.8^\circ$  FWHM. Since this distribution is fairly flat, 2-dimensional skymaps of the angular origins of the showers could be used for source detection, as can be seen from the reconstructed positions in data taken on Markarian 501 in Fig. 8. The errors in angular reconstruction given above are for a single shower; a point source with poorly defined position could thus be localized to  $\sim 1 - 2'$  with the combination of  $\sim 100$  such events.

For the present, a conservative procedure of monitoring the background is used, based on the pointing angle  $\alpha$ , similar to the “orientation” of Whipple [8]:  $\alpha$  is the angle at the image barycentre between the actual source position and the reconstructed source position. The pointing angle does not use the full information contained in the results of the fit, but has a fairly flat distribution from  $0^\circ$  to about  $120^\circ$  for background events, which allows the background

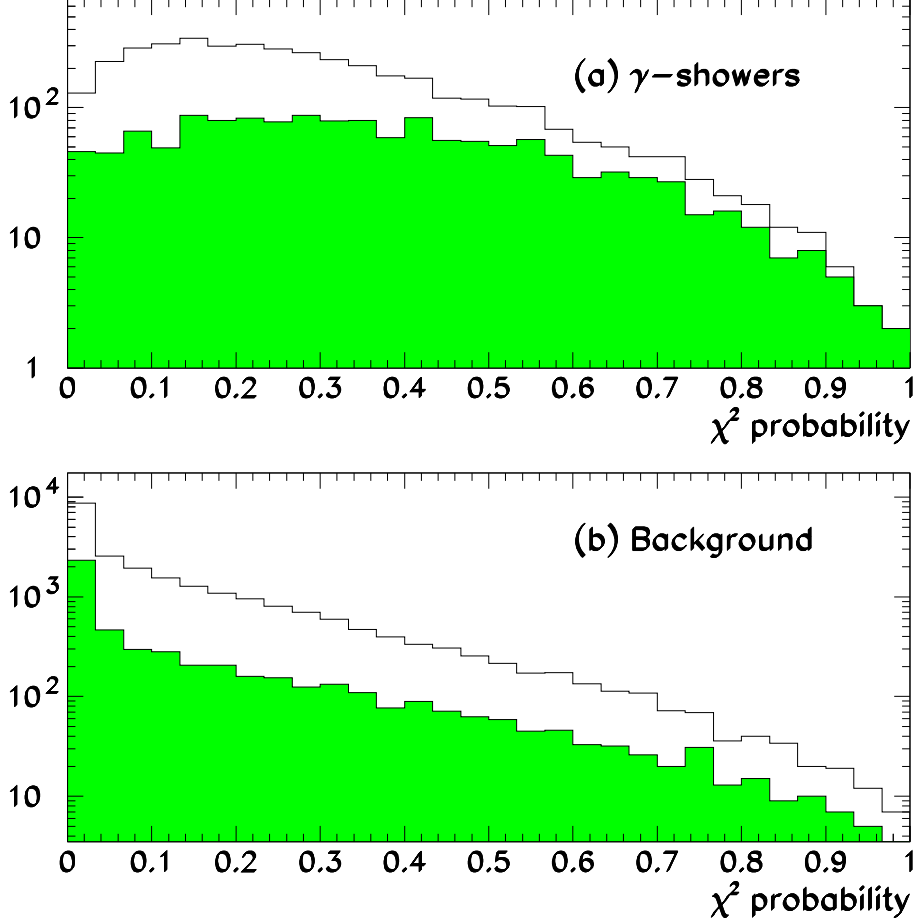


Fig. 6.  $\chi^2$  probability distribution for a fit with the source coordinates considered as free parameters (constraint is from shape alone): a) vertical  $\gamma$ -ray showers; b) real background (off-source data) showers. The upper line in each figure is for all events above threshold, the shaded distributions for events with a fitted energy,  $E_f$ , greater than 350 GeV and a fitted impact parameter,  $D_f$ , between 30 and 125 m.

level to be easily monitored. The cut on  $\alpha$  is more efficient than a cut on the angular distance between the source position and the reconstructed  $\gamma$  origin since, as seen in Fig. 7, the position reconstructed is not symmetric about the source position. The distribution of  $\alpha$  for  $\gamma$ -events from a Crab-like source exhibits a peak at  $0^\circ$  (Fig. 9) and a small accumulation at  $180^\circ$  corresponding to events which are wrongly found to point away from the source. Around 17% of the  $\gamma$ -events from a Crab-like source are in this situation. The proportion of events with a wrongly reconstructed direction decreases with increasing energy, from 22% at 200 GeV to 9% at 600 GeV and 4% at 1 TeV.

The significance of a signal is calculated using the usual formula:  $(ON - OFF)/\sqrt{ON + OFF}$  [19], assuming equal time on and off-source. The significance per hour on a simulated Crab-like source at zenith has been calculated for various cut values on  $\alpha$  and  $P(\chi^2)$  (Fig. 10.a). The best result in terms of both significance and efficiency for  $\gamma$ -events is obtained for a  $P(\chi^2) > 0.2$

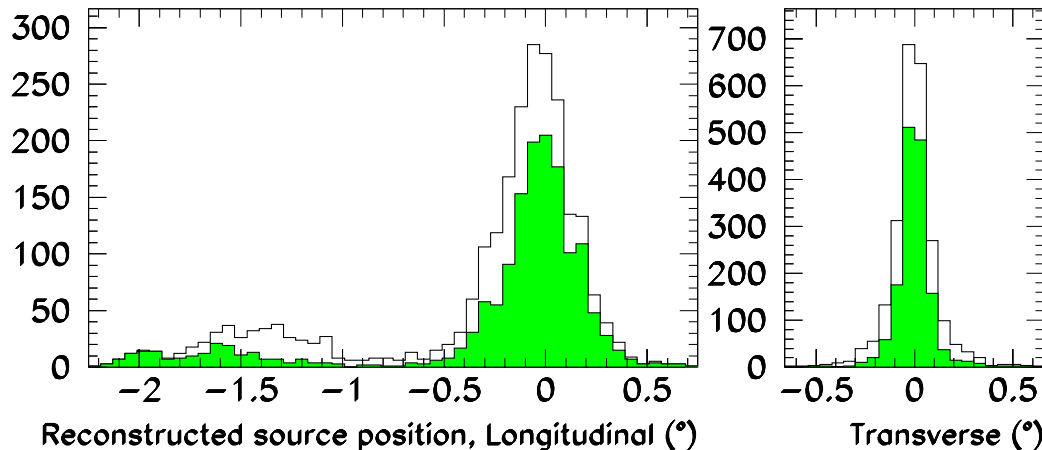


Fig. 7. Distributions of longitudinal and transverse errors (with respect to the image major axis) in the reconstruction of the source position for vertical showers with  $P(\chi^2) > 0.2$ . The small bump at negative values of longitudinal error results from wrong direction reconstruction (mainly for events close to the energy threshold). Shaded histograms correspond to events with a fitted energy greater than 350 GeV.

and  $\alpha < 6^\circ$ , which gives  $5.1\sqrt{t} \sigma$  where  $t$  is the on-source observation time in hours, retaining 34% of the  $\gamma$ -events while giving a rejection factor of 120 on background events. This rejection factor is smaller than for some comparable experiments as there is a large rejection factor at the trigger level, allowing a moderate background rate of 15 Hz at the zenith. At  $45^\circ$  from zenith the best significance for the same cuts falls to  $2.7\sqrt{t} \sigma$ . This is essentially due to the higher energy threshold, leading to a lower event rate; on the other hand, for the same  $\gamma$ -ray selection efficiency the background rejection factor is comparable to that at zenith.

In order to estimate the efficiency of the  $\chi^2$ -method in the case of a source with a poorly-defined position, a simulated Crab-like source has been set on the edge of the trigger area ( $1^\circ$  from the centre). In this case, the equivalent detection area is divided by a factor of the order of two. Even for a source with known position, when the source is not at the centre of the field it is possible to use one side of the camera as the off region for the other side [20]. For a Crab-like source at zenith, the same cuts in  $P(\chi^2)$  and  $\alpha$  as for a source in the centre of the camera give a  $2.3\sqrt{t} \sigma$  significance, with a selection efficiency for  $\gamma$ 's of 36% and a rejection factor of 116 above threshold (Fig. 10.b). This means that the on-source run time has to be five times larger for a source on the edge of the trigger area than for a source at the centre of the field for the same significance. The corresponding significance obtained at  $45^\circ$  from zenith for an off-centre source is  $1.5\sqrt{t} \sigma$ .

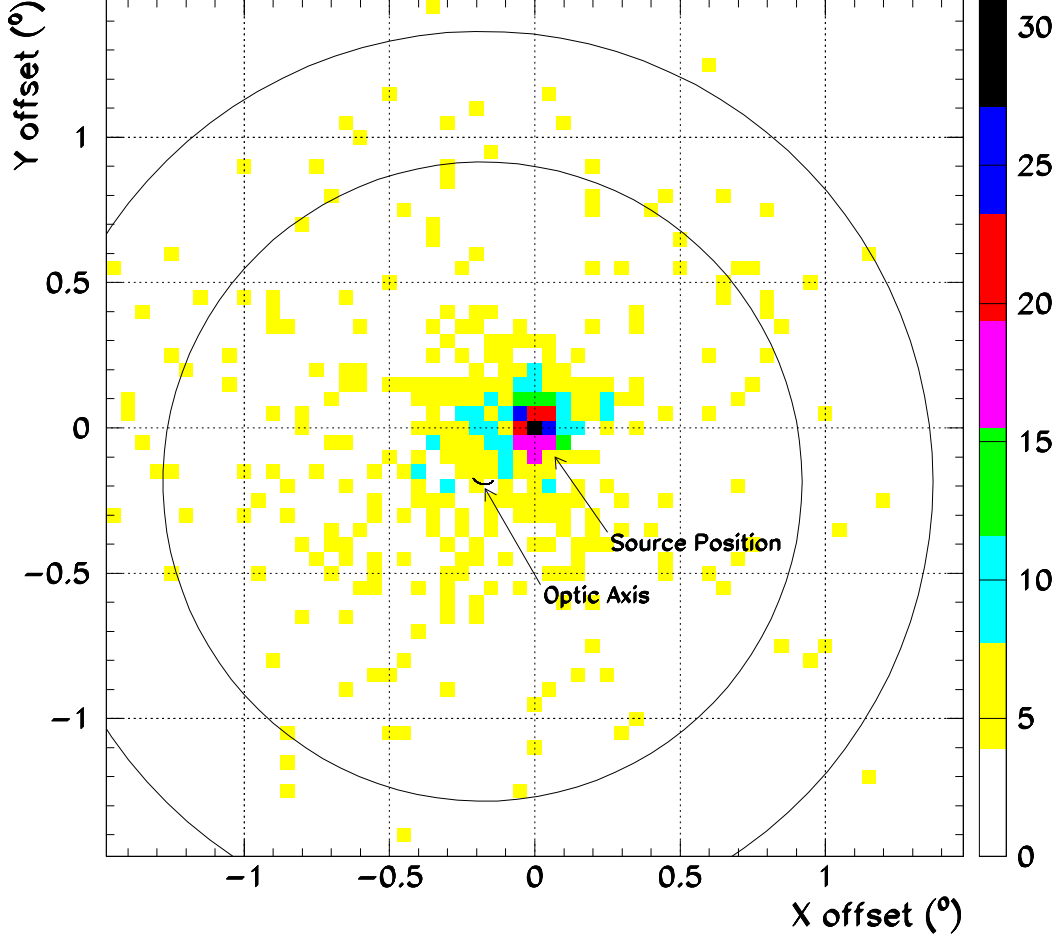


Fig. 8. The distribution of reconstructed angular origins for the data from a 30-minute run on Markarian 501 from April 16, 1997, for events with  $P(\chi^2) > 0.2$ . The concentric circles represent the trigger region and the small-pixel region, respectively. During the run, the optic axis described the small arc indicated due to the mechanical flexibility of the structure, which is monitored as described in [9]. The number of events reconstructed in each bin of  $(0.05^\circ)^2$  is shown. No background subtraction has been performed.

#### 4.2 $\gamma$ -ray energy measurement

For a source detected with a strong enough significance, the energy spectrum can be studied by a detector with good energy resolution. The fit described above in which the source position is a free parameter gives a first estimate of the energy of each event to within about 30%. However, more precise spectral studies can be carried out on point sources of  $\gamma$ -rays. The use of the source position as a constraint in the fit provides a higher accuracy for impact parameter measurement and, as a consequence, for energy measurement. If trigger selection effects are ignored in the Monte-Carlo program (thus accepting all events above 100 GeV), the  $\chi^2$  minimization with respect to  $E_\gamma$ ,  $D$ , and  $\phi$  provides an unbiased energy measurement within about 25% (statistical error

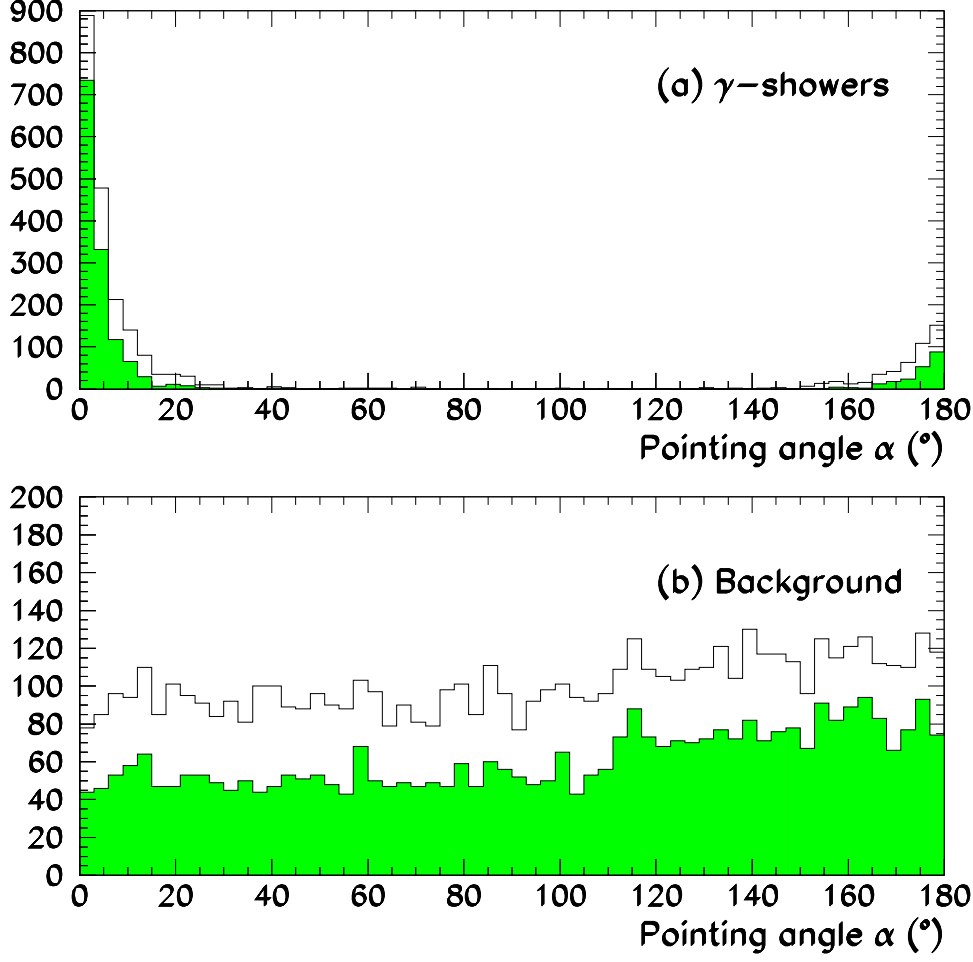


Fig. 9. Distribution of the pointing angle  $\alpha$  for events with  $P(\chi^2) > 0.2$  (constraint from shape alone): a) vertical  $\gamma$ -ray showers; b) Real background (off-source data) showers. The upper line is for all events above threshold, the shaded histograms for events with a fitted energy greater than 350 GeV.

only). Trigger selection effects are small for events well above the threshold, as can be seen for simulated 400 GeV  $\gamma$ -rays in Fig. 11. This figure also shows that the distribution of the fitted event energies about the true energy is Gaussian on a logarithmic scale. Consequently, the slope of a power-law spectrum can be directly estimated with this technique. Close to the threshold, however, the fitted energy  $E_f$  is overestimated as a consequence of the trigger selection. Similarly, the small remaining bias in  $\log(E_f/E_\gamma)$  at 400 GeV is due to showers with large impact parameters for which the trigger selection is critical at this energy since the telescope is then located at the border of the light pool (Fig. 5). This effect is largely removed if only showers with a fitted impact parameter  $D_f$  lower than 125 m are included (shaded histogram in Fig. 11). The bias induced by the trigger selection at different energies is best illustrated by plotting 68% confidence intervals for  $E_f$  as a function of the true value  $E_\gamma$  used in the simulation (Fig. 12). It can be seen that for  $E_f$  below 350 GeV for vertical showers, only an upper limit can be safely derived for  $E_\gamma$ . Therefore,

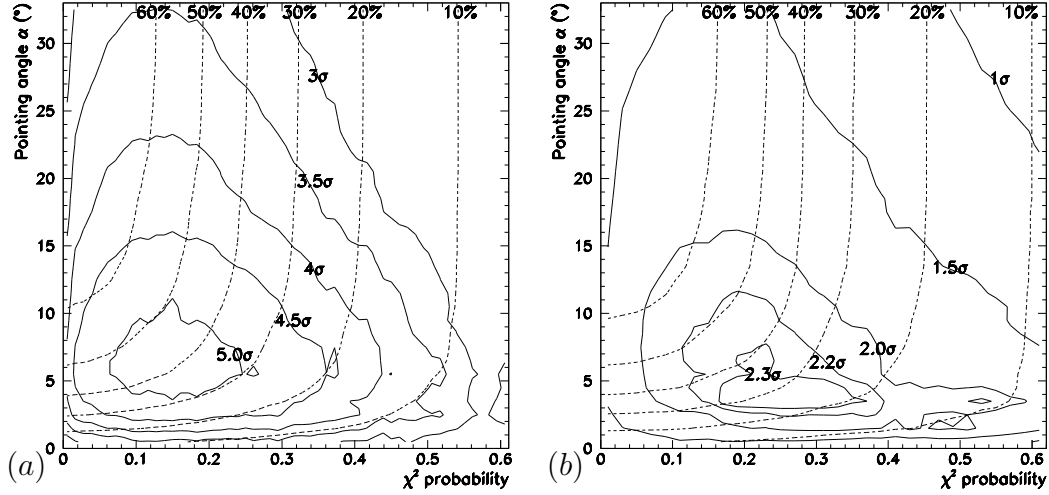


Fig. 10. Detection significance for a Crab-like source at zenith in one hour of observation, shown as a function of the two cuts on  $P(\chi^2)$  and  $\alpha$ : (a) for a source at the centre of the camera; (b) for a source at  $1^\circ$  from the centre. The full lines indicate contours of equal significance; dotted lines show fixed  $\gamma$ -ray selection efficiency.

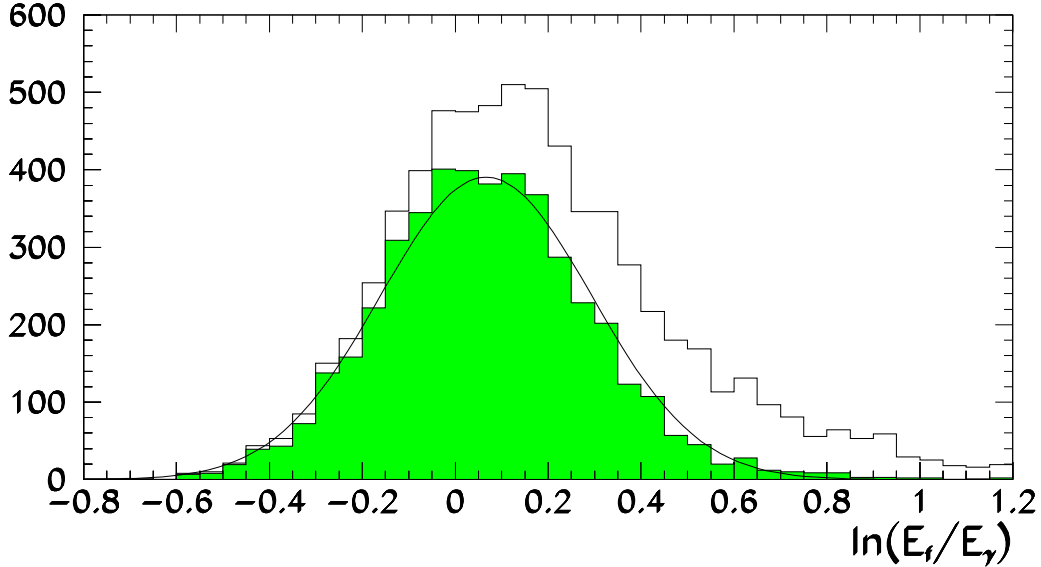


Fig. 11. Distribution of  $\ln(E_f/E_\gamma)$  for vertical 400 GeV  $\gamma$ -ray showers satisfying the selection cuts (the source location,  $\vec{\xi}$ , being fixed in the fit). The shaded histogram is further restricted to events with a fitted impact parameter  $30 \text{ m} < D_f < 125 \text{ m}$ .

spectrum measurement is reliable only above a spectrometric threshold, that is, in the region in which  $E_f$  depends linearly on  $E$ . It is somewhat higher than the nominal threshold which is relevant for source discovery. Fig. 12 also shows the variation of the average values of  $\log(E_f)$  on  $\log(E_\gamma)$  for zenith angles  $0^\circ$ ,  $30^\circ$ ,  $45^\circ$ , and  $60^\circ$ , showing the increase in the spectrometric thresholds with increasing zenith angle. Restricting to events with  $E_f$  above the spectrometric threshold and  $30 \text{ m} < D_f \cos Z < 125 \text{ m}$ , the accuracy of the preceding method is about 20% (statistical error only), independent of the zenith angle  $Z$  up to



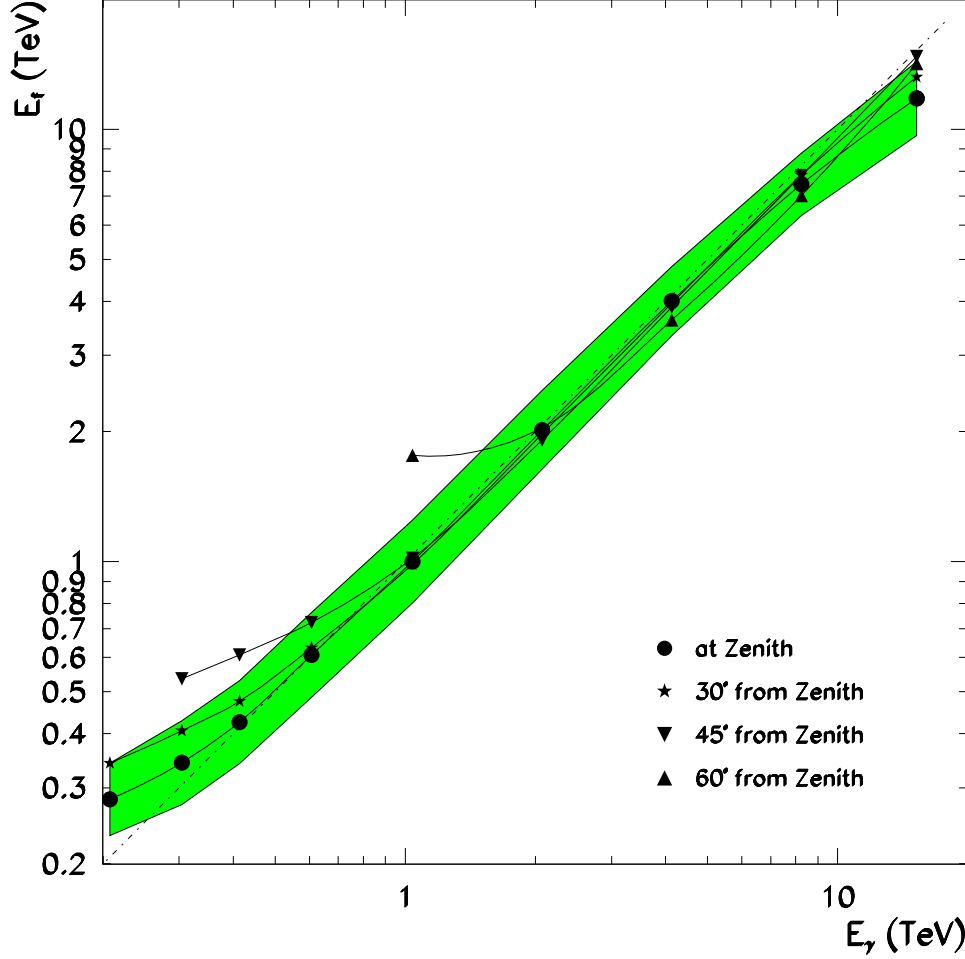


Fig. 12. Fitted energy,  $E_f$ , versus true energy,  $E_\gamma$ , for  $\gamma$ -ray showers satisfying the selection cuts (the source location,  $\vec{\xi}$ , being fixed in the fit) and for which  $30 \text{ m} < D_f \cos Z < 125 \text{ m}$  ( $Z = \text{zenith angle}$ ). The shaded interval shows the 68% confidence intervals for a source at the zenith. The effect of trigger selection on the energy estimation can be seen.

45°.

## 5 Conclusion

The method described above, based on a realistic analytic description of electromagnetic air showers, is best suited for those Cherenkov Imaging Telescopes with a high-resolution camera. The light distribution in the focal plane is fully exploited, yielding the shower direction from the asymmetry of the longitudinal profile as well as the source position in the focal plane. Selection of  $\gamma$ -rays on the basis of the image shape is performed by using a single  $\chi^2$ -variable instead of a series of cuts on various image parameters. By combining the  $\chi^2$  probability cut and a direction ( $\alpha$ ) cut, a significance of  $5\sigma$  per hour can be

achieved for a Crab-like source at the zenith. A future development of the method would be to use the distribution of selected  $\gamma$ -ray origins on the celestial sphere together with the known energy-dependent point spread function of the method to estimate the significance by a maximum-likelihood method. With the CAT telescope (250 GeV threshold), sources with the intensity of the Crab nebula can be detected in one hour. This has been confirmed with the results obtained in the 96/97 observing campaign. Moreover, sources with poorly defined position can be localized with an accuracy of the order of an arc minute on the basis of about 100 showers. The accuracy on  $\gamma$ -ray energy is of the order of 20–25%. Biases induced by the trigger selection have been investigated; in particular, care should be taken in spectrum measurement, which is accurate only above a specific threshold, higher than that used for source detection.

## 6 Appendix 1 : Angular distribution of $e^\pm$ 's in the analytic model

Let  $\theta_e$  be the angle of a charged particle from the shower axis and  $E_e$  its kinetic energy. In [15], the variable of interest is

$$w = \frac{2(1 - \cos \theta_e)}{(E_e/21 \text{ MeV})^2} \quad .$$

In order to be in good agreement with the Monte-Carlo program [10], the average value of  $w$  has been parametrized as

$$\overline{w} = \frac{0.9}{1 + 120 \text{ MeV}/E_e}$$

instead of the corresponding formula given in [15].

## 7 Appendix 2 : Calculation of the mean image longitudinal and transverse profiles

The notation used in the calculation of the semi-analytical model is shown in Fig. 13. The origin  $O$  is taken on the shower axis  $Oz$  as the point closest to the telescope mirror. We consider a charged particle ( $e^\pm$ ) at an angle  $\theta_e$  from the shower axis, with energy  $E_e$ . The  $x$  and  $y$  axes are chosen perpendicular to  $Oz$  in such a way that this particle has no  $y$  component of velocity. The position of the  $e^\pm$  is then given by coordinates  $(x_e, y_e, z_e)$  with  $\overline{y}_e = 0$  and  $\overline{x}_e$  given in [15]. In Fig. 13, point  $E$  represents the  $e^\pm$ 's mean position and the circle centered

on  $O'$  corresponds to Cherenkov light emitted from point  $E$ . As explained in section 3, the telescope mirror is allowed to rotate around  $O$  at distance  $D$  and the corresponding circle intersects the Cherenkov light circle at  $T$  and  $T'$  which are the telescope locations from which the  $e^\pm$  contributes to the image. Consider the location  $T$  and denote by  $\Phi$  the angle  $(Ox, OT)$ ;  $OT$  gives the direction of the image axis in the focal plane and the angular coordinates in this plane (in the longitudinal and transverse direction respectively) are given by:

$$\xi_l = \frac{D - x_e \cos \Phi - y_e \sin \Phi}{z_e - z_T} \quad \xi_t = \frac{x_e \sin \Phi - y_e \cos \Phi}{z_e - z_T}$$

where  $z_T$  is the  $z$ -coordinate of the telescope. In order to include the contribution of position fluctuations, a semi-empirical procedure has been used. If the charged particle position  $(x_e, y_e)$  is allowed to have a spread around  $E$  of  $\sigma_x$  and  $\sigma_y$  (as given in [15]), the Cherenkov light circle does not always intersect the circle centered on  $O$  with radius  $D$ ; this results in an apparent reduction of  $\sigma_x$  and  $\sigma_y$ . Therefore, the image transverse spread  $\sigma_t$  due to the preceding  $e^\pm$ 's is evaluated as follows:

$$\sigma_t^2 = \alpha^2 \frac{(\bar{x}_e^2 + \sigma_x^2) \sin^2 \Phi + \sigma_y^2 \cos^2 \Phi}{(z_e - z_T)^2}$$

where  $\alpha$  has been adjusted to the value  $\simeq 0.5$  in order to agree with the results of Monte-Carlo calculations. The form of this semi-empirical formula is not critical to the method, since the pixel size is much greater than  $\sigma_t$ .

In the calculation of the longitudinal profile,  $\xi_l$  is calculated for  $x_e = \bar{x}_e$  and  $y_e = 0$ . The linear density of Cherenkov light along the image axis is given by summing over the  $e^\pm$ 's, i.e. over  $\theta_e$ ,  $E_e$ , and  $z_e$  at fixed  $\xi_l(\theta_e, E_e, z_e)$ :

$$\frac{dN}{d\xi_l} = \iiint_{\xi_l = \xi_l(\theta_e, E_e, z_e)} \frac{\partial^2 N_e}{\partial \theta_e \partial E_e} \frac{dL}{dz_e} P d\theta_e dE_e dz_e$$

where  $\partial^2 N_e / (\partial \theta_e \partial E_e)$  gives the angular and energy distributions of the  $e^\pm$ 's,  $dL/dz_e$  is the amount of Cherenkov light emitted per unit track length and  $P$  is the fraction of this light which, on average, reaches the mirror:

$$P = \frac{\delta\omega}{\pi} \frac{S}{4\pi DR}$$

where the first ratio is the fraction of Cherenkov light impinging on the mirror at  $T$  (the angle  $\delta\omega$  is defined in Fig. 13) and the second the probability to find the mirror (with area  $S$  and radius  $R$ ) around  $T$ . Similarly, the square

of the overall transverse spread of the image  $\Sigma_t$  for a given value of  $\xi_l$  is obtained by averaging  $\sigma_t^2(\theta_e, E_e, z_e)$  over  $\theta_e$ ,  $E_e$ , and  $z_e$  at fixed  $\xi_l(\theta_e, E_e, z_e)$ . The light calculated in a given interval of  $\xi_l$  is considered to be distributed in the transverse direction as indicated by the following formula, scaled to the calculated spread  $\Sigma_t$ :

$$F(\xi_t) = \frac{1}{\sqrt{2}\Sigma_t} \exp\left(-\frac{\sqrt{2}|\xi_t|}{\Sigma_t}\right) \quad .$$

## Acknowledgements

The authors are grateful to the French and Czech ministries of Foreign Affairs for providing grants for physicists' travel and accommodation expenses.

## References

- [1] Cawley M.F. *et al*, Exper. Astron. **1**(1990)173.
- [2] Hara T. *et al*, Nucl. Inst. and Meth. **A332**(1993)300.
- [3] Daum A., *et al*, Astroparticle Phys.,**8**(1997)1.
- [4] Vacanti G. *et al*, Ap.J. **377**(1991)467.
- [5] Kifune T. *et al*, Ap.J. **438**(1995)L91.
- [6] Punch M.*et al*, Nature **358**(1992)477.
- [7] Quinn J. *et al*, Ap.J. **456**(1996)L83.
- [8] Punch M. *et al*, Proc. 22<sup>nd</sup> ICRC, Dublin, Ireland, **1**(1991) 464.
- [9] Barrau A. *et al*, Nucl. Inst. and Meth., accompanying paper (1998).
- [10] Kertzmman M.P. and Sembroski G., Nucl. Inst. and Meth. **A343**(1994)629.
- [11] Punch M., "Towards a Major Atmospheric Cherenkov Detector III", Tokyo, Japan, ed. T. Kifune, Universal Academy Press, Inc. Tokyo (1994) 215.
- [12] Goret P. *et al*, "Towards a Major Atmospheric Cherenkov Detector V", Kruger National Park, South Africa, (in press) and Astro/ph 9710260.
- [13] Degrange B., "Towards a Major Atmospheric Cherenkov Detector II", Calgary, Canada, ed. R.C. Lamb, Iowa State University (1993) 215.
- [14] Goret P. *et al*, Astron. Astrophys, **270**(1993)401.

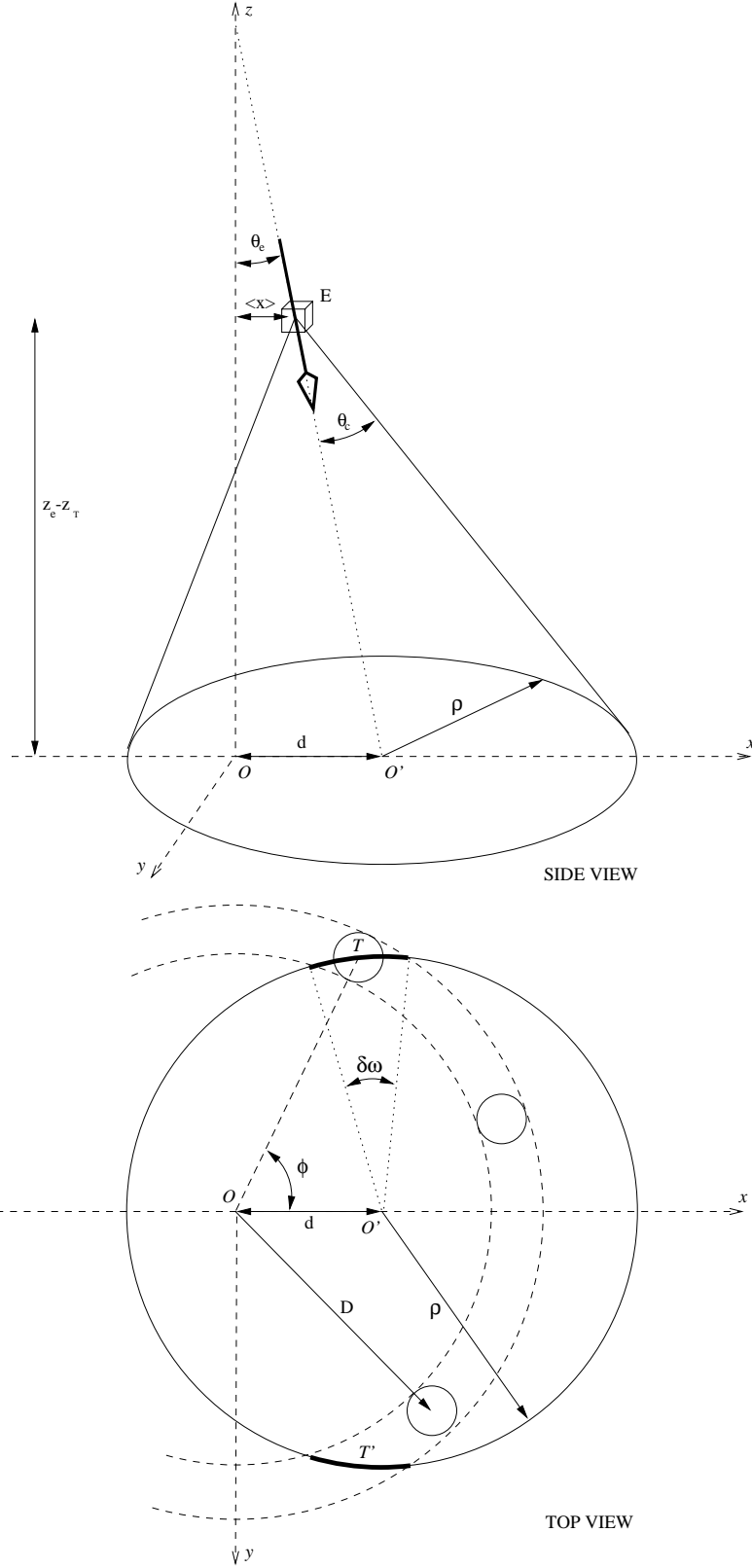


Fig. 13. Geometric construction used in the derivation of the semi-analytical model. See Appendix 2 for explanation.

- [15] Hillas A.M., J. Phys.G: Nucl. Phys. **8**(1982)1461.
- [16] Sarazin X., Doctoral Thesis, Université d'Aix Marseille II, unpublished (1994).
- [17] Fichtel C.A. *et al*, Ap.J. Supp. **94**(1994)551.
- [18] Akerlof C.W. *et al*, Ap.J. **377**(1991)L97.
- [19] Li T., Ma Y., Ap.J. **272**(1994)317.
- [20] Fomin V.P. *et al*, Astroparticle Phys. **2**(1994)137.